Conformational maps of human 20S proteasomes reveal PA28- and immuno-dependant inter-ring crosstalks

Jean Lesne[1,†#], Marie Locard-Paulet[1,2#], Julien Parra[1], Dušan Zivković[1], Marie-Pierre Bousquet[1], Odile Burlet-Schiltz[1] and Julien Marcoux[1]*

[1]Institut de Pharmacologie et de Biologie Structurale (IPBS), Université de Toulouse, CNRS, UPS, Toulouse, France.
[2]Novo Nordisk Foundation Center for Protein Research, University of Copenhagen, Denmark.
Present Address: [†]Centre de Biochimie Structurale, CNRS, Université de Montpellier, INSERM, 34090 Montpellier, France.
[#]J.L. and M.L.P. contributed equally to this work. *To whom correspondence should be addressed. Email: julien.marcoux@ipbs.fr.

Abstract

Here, we used for the first time Hydrogen-Deuterium eXchange coupled to Mass Spectrometry (HDX-MS) to investigate conformational differences between the human standard 20S (std20S) and immuno 20S (i20s) proteasomes alone or in complex with PA28αβ or PA28γ activators. Their solvent accessibility (in the form of deuteration kinetics) were analysed through a dedicated bioinformatic pipeline including stringent statistical analysis and 3D visualisation. These data confirmed the existence of allosteric differences between the std20S and i20S at the surface of the α-ring triggered from inside the catalytic β-ring. Additionally, binding of the PA28 regulators to the 20S proteasomes modified solvent accessibility due to conformational changes of the β-rings. This work is not only a proof of concept that HDX-MS can be used to get structural insights on large multi-protein complexes in solution, it also demonstrates that the binding of the std20S or i20S subtype to any of its PA28 activator triggers allosteric changes that are specific to this 20S/PA28 pair, in terms of the regions affected. Data are available via ProteomeXchange with identifier PXD018921.

Introduction

The ubiquitin proteasome system (UPS) is central to proteostasis. Its most downstream element is the 26S proteasome, which is responsible for protein degradation. Specifically, the proteasome clears the cells of abnormal, denatured or in general damaged proteins and regulates degradation of short-lived proteins that are in most cases conjugated to ubiquitin. The 26S proteasome is a highly conserved compartmentalized multi-catalytic protease complex composed of more than 30 subunits and consists of two main complexes: the 20S catalytic core and the 19S regulatory complex. As the proteasome activity is directly involved in the intracellular concentration of many cytokines and hub proteins, and may generate immunogenic peptides, it is the focus of intense regulation according to cell needs, and dynamically localizes within cells in response to physiological and external perturbations[1,2]. Numerous pathologies are directly due to the genetic polymorphism of the proteasome including cancer, heart disease, Proteasome Associated Autoinflammatory Syndrome, lipodistrophy, type 2 diabetes to name a few (reviewed in[3]).

The main mechanism regulating the proteasome activity is the substitution of the constitutive catalytic subunits β1, β2 and β5 of the standard 20S (std20S) with other subunits. For example, the immunoproteasome (i20S) contains the immuno-subunits β1i, β2i and β5i that have different cleavage specificities and are known to generate immunogenic peptides[4]. It is strongly expressed in cells of the immune system and can be induced in most tissues by interferon-γ (IFN-γ). Similarly, the thymoproteasome, exclusively found in thymus, contains the β1i, β2i and β5t subunits. This particular

subunit composition generates peptides responsible for the positive selection of CD8+T cells in thymus[5].

The proteolytic activity of the 20S proteasome is also regulated by its interaction with different regulators, the most common being the ATP-dependent 19S activator that is involved in the UPS degradation pathway. However, less abundant ubiquitin-independent regulators such as PA28αβ, PA28γ or PA200 are also known to activate the 20S and modify its substrate specificity. New regulators are still being discovered on a regular basis, as it was the case recently for NQ01 and DJ-1 under oxidative stress[6,7]. In addition, a vast collection of Proteasome Interacting Proteins (PIPs) regulate or assist proteasomal functions[8–12].

Besides its subunit composition and association with regulators and/or PIPs, the proteasome is subjected to a wide variety of post-translational modifications (PTMs) affecting its subunits activity[13,14]. Our team developed numerous tools to study the structural diversity of proteasomes and their regulators by bottom-up proteomics in a variety of biological materials ranging from cell lines, biopsies and organs. The study of the 20S proteasome showed the presence of at least 32 isoforms for the α1-7 and β1-7 subunits[15]. The literature reports 57 and 83 PTMs on the 20S subunits and 19S regulator, respectively (human, bacteria and yeast)[13]. These data illustrate the highly heterogeneous and dynamic nature of the proteasome, which provides the catalytic flexibility required to regulate such a central cellular system.

The combination of these three levels of regulation (catalytic subunits, regulators, PTMs) implies a wide proteasome subtype heterogeneity. This diversity probably results in specialized functions of each individual proteasome form, providing various means to adapt protein degradation pathways to changing conditions in the cell. Today's challenges are (i) to correlate the subunit composition and/or presence of specific PTMs with the associated regulators and (ii) to understand how the different subtypes of proteasome influence its proteolytic activity and the function of the cell.

To answer these questions, the proteasome has been intensely studied from a structural and functional point of view, since its discovery in 1988[16]. A large part of the structural studies was achieved by electron microscopy (EM), enabling amongst others to observe the 20S in complex with different regulators[17–22] and to characterize certain catalytic intermediate-states of the 26S[23]. The combination of cryo-EM and covalent cross-linking coupled to mass spectrometry (MS) allowed to refine the structure of these different catalytic intermediates[24,25] and to propose structural models in complex with different partners, including the 19S[19], Ecm29[12] and other PIPs[12]. X-ray crystallography also provided high-resolution structures of proteasomes alone or in the presence of covalent inhibitors[26], regulators[27,28], and complexes of proteasome with their associated regulators[12,26,27].

The size of the complex is obviously a limit for its analysis by Nuclear Magnetic Resonance (NMR). However, it was possible to resolve the structure of the eukaryotic proteasome from *Thermoplasma acidophilum* that contains only one type of subunit α and β. It showed evidence of a conformational change of the catalytic sites located in the center of the proteasome upon binding of a regulatory particle on its surface, which can be described as an "outer-to-inner" allosteric change[29]. A reverse "inner-to-outer" change was also observed at the binding interface when modifying the catalytic site. This "inner-to-outer" conformational change was not observed when comparing the X-ray structure of the std20S[30] (PDB 5LE5) with the recent X-ray[31] (PDB 6E5B) and cryo-EM[32] (PDB 6AVO) structures of the i20S (RMSD=0.392 Å and 0.480 Å, respectively). However, the "outer-to-inner" mechanism was recently shown in human by comparing the cryo-EM structures of the 20S with and without PA200[21] as conformational changes were found not only at the binding interface (opening of the pore), but also down to the catalytic sites.

Despite such great achievements, these high-resolution methods are still limited by either the size, the heterogeneity, or the dynamics of the purified complexes. This is evidenced by the small number of structures of the 20S bound to regulators and by the numerous missing regions (too dynamic) in these resolved structures. The emergence of native MS contributed to a better understanding of the 20S assembly mechanism[33] and of the architecture of the 19S lid[34] as well as the identification of new partners of the 20S proteasome extracted from rat liver[6,7]. More recently, top-down MS, consisting in the analysis and fragmentation of entire proteins in the gas-phase[35] was applied to the proteasome in order to deeply characterize the proteoform[36] landscape of the 20S α and β subunits[37,38].

In this work, we optimized an emerging structural MS method called Hydrogen-Deuterium eXchange coupled to MS (HDX-MS) in order to investigate the binding interfaces and structural rearrangements upon binding of the PA28 regulators to the standard 20S (std20S) and immuno 20S (i20S). This isotopic labelling technique not only allows to differentiate flexible and/or accessible from rigid and/or protected regions of a complex, but also to identify interaction surfaces and to spot allosteric conformational changes in solution. We present here the first HDX-MS analysis of the entire human std and i20S core particles as well as their PA28αβ and PA28γ regulators, providing solvent accessibility/dynamics information for each one of these complexes. Comparison of the std *vs.* i20S shows interesting differences and further differential analysis of the core particles with and without their regulators provide a molecular rationale for their differential interactions. Our data provide evidences for the "inner-to-outer" allosteric change of the human 20S upon incorporation of the immuno-subunits and the reverse "outer-to-inner" transduction signal upon PA28 binding, illustrating the interplay between the different proteasome regulation pathways. Altogether, this work highlights the potential of HDX-MS as a new tool to get low resolution but very informative structural information on such large oligomeric complexes. It opens the door to many other applications of the technique, including identifying PIPs binding surfaces and investigating the stabilizing/destabilizing effects of small-molecules or protein-based regulators of the 20S activity.

Results

Development of a HDX-MS pipeline dedicated to the comparative analysis of 20S proteasome/regulator complexes

HDX consists in the exchange of backbone amide hydrogens (H) with deuteriums (D) in proteins in solution. The rate of exchange depends on the accessibility to the solvent and/or the flexibility of a given region, thereby providing low resolution but crucial information on the protein conformation. In a classical HDX-MS workflow (**Fig. 1A**), the proteins of interest are digested online and the generated peptides are separated on a reverse phase column before MS analysis to monitor deuterium incorporation rates.

The main challenges encountered when analysing heterogeneous complexes such as the proteasome are threefold. First, the high number of peptides generated after digestion entailed specific optimization of their chromatographic separation. Second, we optimized the quenching step and injection parameters to reduce dead-volumes, as well as the acquisition method, in order to handle samples at low concentration (<1 µM) (see material and methods for a more detailed description of the optimized parameters). Finally, we developed a computational pipeline dedicated to the multi-dimensional analysis of HDX-MS analysis of large complexes. The resulting data were mapped to available 3D structures using our recently developed open-source web application HDX-Viewer[39].

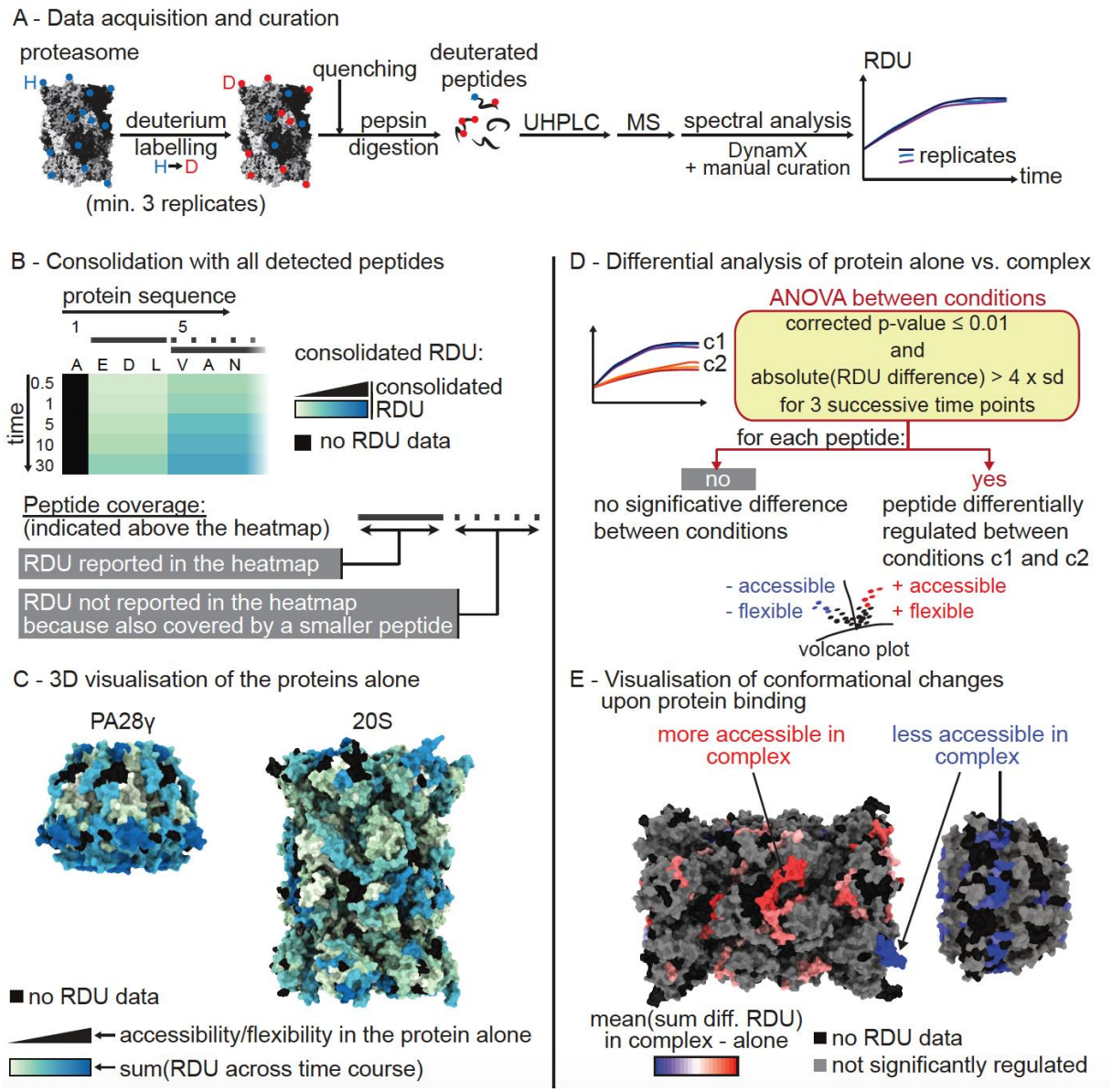

Figure 1. HDX workflow applied to the analysis of the 20S proteasome and its regulators. (A) Workflow applied for HDX sample preparation, data acquisition, inspection and curation. **(B)** Consolidation: projection of peptide RDUs to the protein sequence was performed by mapping the RDU values of the smallest peptides (solid lines) to the amino-acid portions they cover on the protein sequence. The RDU of the longer peptides were not reported on the heatmap (dashed lines). **(C)** Visualisation of the solvent accessibility of the protein analysed alone through mapping of the sum of consolidated RDUs across all time points to their 3D structure. **(D)** Statistical analysis applied to the comparison of proteins alone or in complex (20S + PA28). **(E)** 3D visualisation of the differences of RDU measured between the proteins alone or in complex. The consolidation is performed as described in (B) with the sum(mean difference of RDUs per time point). "H": hydrogen; "D": deuterium; "diff.": difference; "RDU": relative deuterium uptake.

We worked with commercial std20S and PA28αβ from human erythrocytes, i20S from human spleen and recombinant human PA28γ produced in *Escherichia coli*. Our experimental setup consisted in triplicate labelling of PA28αβ, PA28γ, the std20S or the i20S alone, or with a 2-fold molar excess of PA28αβ or PA28γ (std20S+PA28αβ / std20S+PA28γ / i20S+PA28αβ / i20S+PA28γ) for 0, 0.5, 1, 5, 10 and 30 min (144 independent samples). The isotopic motifs of each peptide, at each time point and in each condition were automatically extracted by the DynamX software and subjected to manual curation to control that the assignments were correct, and re-assign the peaks if needed. This step was

probably the most time-consuming as we manually checked 767 peptides, corresponding to approximately 400,000 isotopic envelopes. Peptide kinetics of deuterium uptakes were then calculated and subjected to statistical analysis before consolidation (mapping of the peptide relative deuterium uptakes to the protein amino-acid sequence) and visualisation onto 3D structures and/or models for biological interpretation (**Fig. 1B-E**).

We performed two distinct analyses: (i) the identification of the most accessible and/or dynamic regions of the proteins in solution (**Fig. 1B-C**), and (ii) the differential analysis of each protein alone or in complex (**Fig. 1D-E**). For the second, we performed an ANOVA between the kinetics of deuterium incorporation in the two conditions compared and considered peptides significantly regulated if they presented a corrected p-value ≤ 0.01 and absolute difference of relative deuterium uptake > four times the standard deviation (**Fig. 1D**). The consolidated data were then plotted onto 3D structures when available. For the differential analyses, we visualised the sums of differences across time points of relative deuterium uptakes between conditions for peptides passing the statistical thresholds (**Fig. 1E**). This allowed the identification of regions presenting significant differences of deuteration, which indicates a modification of their solvent accessibility upon complex formation that can be due to the presence of a binding interface or to allosteric changes. This approach was used to identify the conformational differences between the std20S and i20s; and to compare their structural changes upon binding to PA28αβ or PA28γ.

Dynamic interfaces uniting the 4 rings of the 20S proteasome

Thanks to thorough workflow optimizations, we obtained 89% subunit sequence coverage on average for all the 17 subunits of the std20S and i20S (**Fig. S1-S2, Table S1** for sequence coverages and **Table S2** for RDU of each peptide of the proteins alone). We then mapped our HDX-MS results on the 3D structure of the human std20S (PDB: 5LE5, **Fig. 2A-B**). As expected, we globally found a faster and higher deuteration of the solvent facing α-ring interface of the std20S (**Fig. 2C**) compared to any other of its ring interfaces. This observation benchmarks our approach by confirming that high relative deuteration uptakes directly indicate which regions of the proteasome are more dynamic and potentially accessible for interaction with regulators or PIPs. The N-terminal (N-ter) part of the α-subunits constituting the α-ring were highly deuterated. The only exception, α3, was due to its N-ter peptide not being detected (**Fig. S3,** in black). According to the 3D structure of the std20S, these N-ter are located around the proteasome pore entry, and their high deuterium uptake strongly supports the hypothesis of a flexible pore entrance in the std20S that fluctuates between open and closed states[40–42] (**Fig. 2C**).

Other dynamic/accessible regions of the α-ring include some very dynamic patches made of non-contiguous peptides from the same subunit like α3 (176-186/238-261), α4 (44-54/197-206), and α5 (49-63/167-181) (**Fig. 2C**). We expect that these regions can interact with the many different PIPs. Our analysis also identified dynamic patches at the interface between different subunits, as it is the case between α1 (2-22/165-178) & α2 (194-202), α3 (176-186) & α4 (44-54) and α5 (167-181) & α6 (48-56), corresponding to the 1-2, 3-4 and 5-6 α-pockets[43] that are known to accommodate the C-terminal (C-ter) tails of Rpt3, Rpt2 and Rpt5, respectively[19,43]. However, the outer surface of α2, which is in close proximity to Rpt11 in the 26S[19] was not particularly dynamic in our data. We also identified patches of flexible regions on the interface of the α-ring facing the β-ring (**Fig. 2D**), where amino acid stretches of α4 (91-102), α5 (102-107) and α7 (140-148) were slightly more flexible than the rest of the interface (**Fig.2D** and **Fig.S3**).

The β-ring was globally less deuterated than the α-ring (**Fig. 2E-F**), which was expected since it does not present a large interface with the solvent. After 30 seconds of deuteration, the interface facing the α-ring (**Fig. 2E**) was particularly poorly labelled (**Fig. S3**). However, after 30 minutes, some bulges facing the α-ring were moderately deuterated in all β subunits but β7 (red circles in **Fig. 2E**, and **Fig. S3**). These are composed of the loops located between the α-helices 1 and 2 of each monomer (β1 66-82, β2 67-79, β3 75-87, β4 68-79, β5 67-77 and β6 74-91) as well as some loops between the β-strands 4 and 5 of β4 (37-40) or between the β-strands 6 and 7 of β2 (105-110). It is interesting to note that some of these dynamic loops of the β-ring are facing highly deuterated regions of the α-ring described above and define flexible regions of the α-ring/β-ring interface.

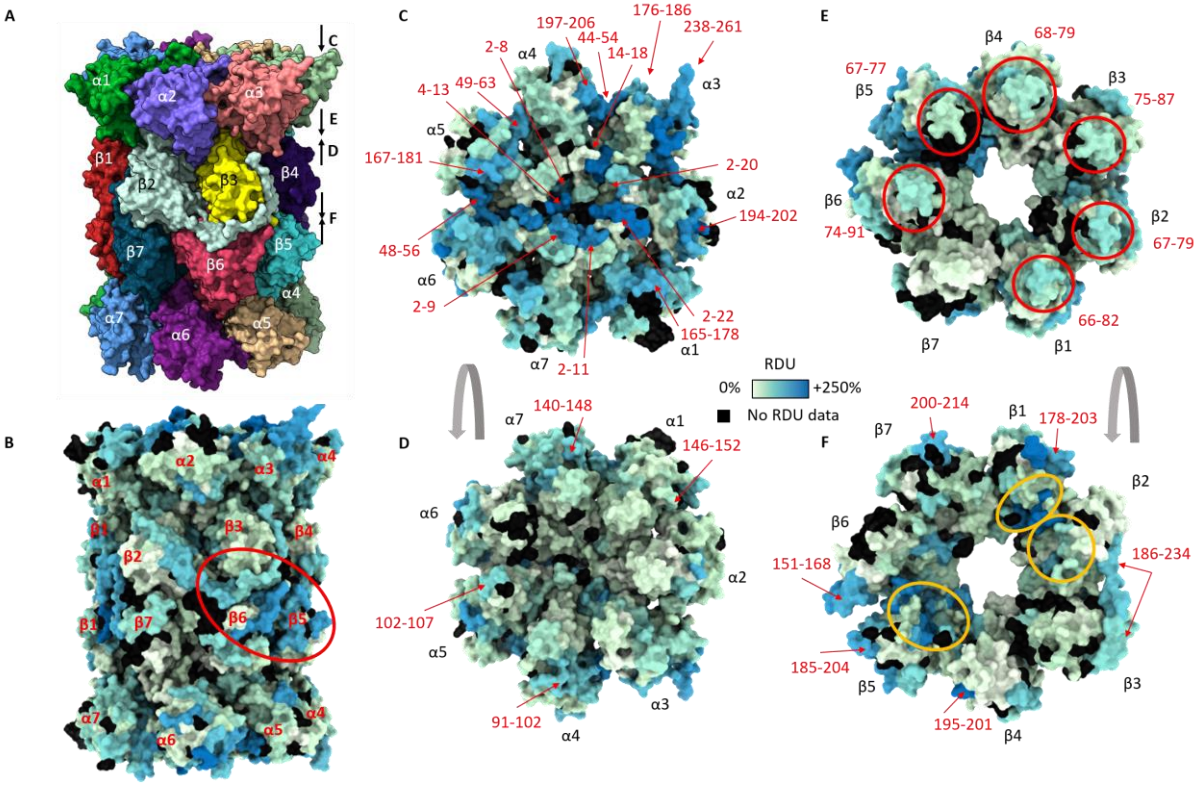

Figure 2. HDX-MS of the std20S reveals a dynamic pore entrance and inter-ring interface. **(A-B)** Structure of the human std20S proteasome (PDB: 5LE5)[30] showing the four stacked αββα heptameric rings colored by subunit **(A)** or relative deuterium uptake (RDU) **(B)**. **(C-F)** Their solvent accessibility is represented on each face of the α-ring (solvent interface **(C)** and β-ring interface **(D)**) and β-ring (α-ring interface **(E)** and β-ring interface **(F)**) as the sum of consolidated relative deuterium uptakes between 0.5 and 30 min. Regions discussed in the text are indicated with red arrows and the moderately flexible/accessible bulges at the interface between the α- and β-ring are circled in red in **(E)**. The corresponding residues are indicated in red around the structures. Active sites are circled in orange **(F)**. The ring faces visualized in D to F are indicated by arrows on the right of the structure in **(A)**.

The most dynamic regions of the β-ring were located on its outer surface (exposed to the solvent) and were constituted of the C-ter of β1 (178-203), β2 (186-234), β4 (195-201), β5 (185-204) and β7 (200-214) as well as loops between β-strands and α-helices, particularly between helices 4 and 5 of β1 (144-152), β4 (145-156), β5 (141-152), β6 (151-168) and β7 (152-167) (red circles in **Fig. 2F** and **Fig. S3**). These regions are particularly interesting since they can potentially interact with the numerous PIPs described in the literature. Our data indicate two symmetrical dynamic patches on each side, at the interface between the β-rings (**Fig. 2F**, **Fig. 2B**, circled in red). These are constituted by the highly flexible interface between β5 and β6 and the nearby C-ter part of β2 (from the opposite β-ring), which protrudes and forms an extended loop enveloping β3 (**Fig. 2A-B**).

Conformational differences between the std and i20S active sites and substrate pockets 1, 2 and 3.

Our data indicate that the catalytic chamber of the std20S that is localised at the β-ring/β-ring interface is locally very flexible (**Fig. 2F and Fig. 3**). The residues forming the S1 and S2 pockets[26] of the β1 were highly deuterated, together with the T23 of the S3 pocket (**Fig. 3B**). The catalytic residues of the β2 subunit remained poorly deuterated compared to the other residues of this subunit (**Fig. 3C**), with the exception of the residues 45-53 that constitute the S1 and S2 pockets of β2. β5 was globally more deuterated than the other subunits of the std20S. Most of the residues forming its catalytic site and substrate pockets were highly deuterated (**Fig. 3D**). Notably, the two residues forming its S' pocket were poorly deuterated.

The direct comparison of the deuteration rates between the standard and immuno catalytic subunits (β1/β1i, β2/β2i and β5/β5i) was not possible due to sequence differences. Moreover, we obtained a relatively poor sequence coverage of the immuno-specific subunits compared to the rest of the data set (**Fig. S3** and **Table S1**). This hindered further direct comparison of solvent accessibility between the catalytic subunits. For example, we cannot comment on the accessibility of the S1, S2 and S3 pockets of β2i (**Fig. 3B**). Nevertheless, our data showed that the residues T20 (pocket S1) and T22 (pocket S3) of β1 were more deuterated than the corresponding region of β1i (**Fig. 3B**). The active site and S1 pocket of β5 also appeared more flexible in the standard than in the immuno-specific subunit (**Fig. 3D**). Although limited, these data inform on the differences of flexibility of the std and i20S catalytic sites.

An inner-to-outer conformational change upon substitution of standard to immuno-specific subunits

The comparison of the structures of the i20S and std20S catalytic subunits from mice show that, although these possess very similar β2 and β2i substrate binding channels, their S1 and S3 substrate pockets are smaller in β1i compared to β1; and β5i possesses smaller S2 and S3 pockets whereas its S1 pocket is larger than in β5[26]. However, very little structural difference is found between the i20S and std20S as far as the α subunits and non-catalytic β subunits are concerned (Root-Mean Square Deviation of the Cα < 0.72 A°). The same is true when comparing the recent structure of the human i20S (PDB 6E5B[31]) with the std20S (PDB 5LE5) (RMSD of the Cα < 0.67 Å). The fact that the inner-to-outer allosteric change observed on a prokaryotic 20S by NMR[29] could not be seen in these crystallographic structures could be inherent to the method (crystal packing). In order to confirm or infirm this inner-to-outer allosteric change, we compared the relative deuterium uptakes of all the non-catalytic subunits of the i20S with those of the std20S. The relative deuterium uptakes of the i20S alone are available in **Fig. S2, S3** and **Table S2**.

The differences in solvent accessibility of the catalytic and substrate pockets between the std20S and i20S translated to significant conformational changes on the non-catalytic subunits of the proteasome core particle. The results of our statistical analysis are presented in **Fig. 4** where the structure of the std20S is color-coded with the sum of relative deuterium uptake differences in the two 20S (i20S - std20S) (see **Fig. S2** for full kinetics, **Fig. S4** for heatmap visualisation, **Fig. S5** for volcano plots, **Table S3** for the list of regions that pass our statistical thresholds and **Table S4** for the outputs of the statistical analysis). Overall, the non-catalytic β-ring subunits were more dynamic in the i20S than in the std20S, with more than 50 peptides significantly more deuterated (**Fig. 4A-B** in red, **Fig. S4-S5**). The β-ring/β-ring interface and the inside of the β-ring were particularly more dynamic/accessible in the i20S compared to the std20S (**Fig. 4A** and **Fig. S4**), together with two bulges of β6 and β7 facing the α-ring (**Fig. 4B**, red circles). Four bulges of α2/3/5/6 facing the β-ring were also significantly more dynamic in the i20S compared to the std20S (**Fig.4C**, red circles).

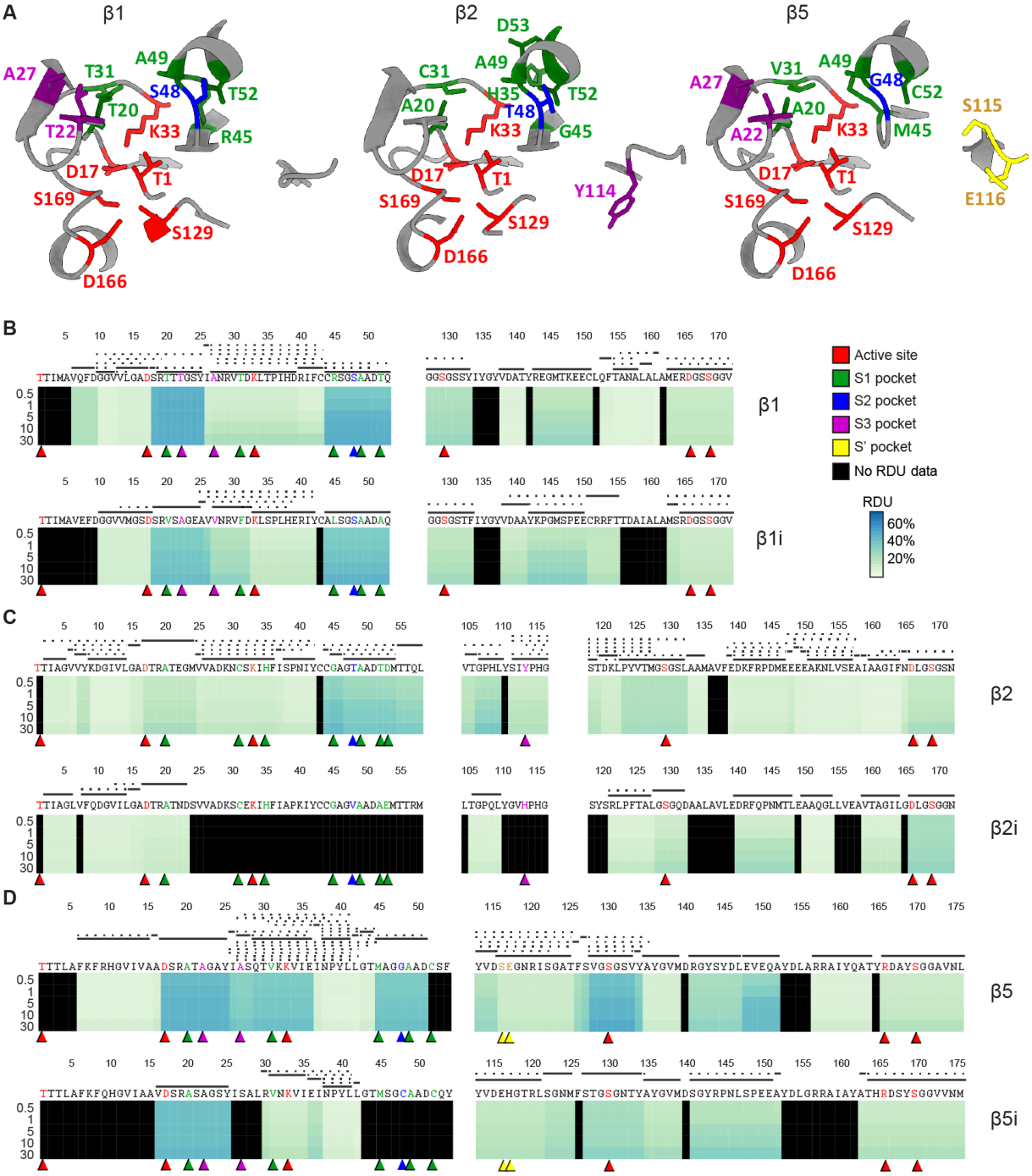

Figure 3. Comparison of the catalytic subunit solvent accessibilities. (A) Representation of the three catalytic subunits β1 (left), β2 (middle) and β5 (right) of the std20S (PDB: 5LE5). The residues forming the active site and the substrate-specific pockets are indicated and color-coded (active site, S1, S2, S3 and S' are represented in red, green, blue, purple and yellow, respectively). **(B-D)** Deuteration heatmaps showing the relative deuterium uptake (RDU) for each timepoint of the kinetics, along the protein sequences of β1/β1i **(B)**, β2/β2i **(C)** and β5/β5i **(D)**. The peptide sequence coverage is presented above the heatmaps as explained in **Fig. 1B**. For the sake of clarity, only the stretches containing residues of the active sites and substrate pockets are represented here.

The only region of the β-ring that was significantly more accessible in the std20S was the 152-167 stretch of β7, located on the external side of the ring (**Fig. 4A**). Its difference of deuteration kinetics could be explained by the fact that this portion of β7 is in direct contact with the β2 or β2i subunit of the other β-ring (**Fig. 2A**). Although far from the catalytic subunits of the β-ring, the pore entrance on the solvent-accessible surface of the α-ring (N-terminal residues of the α subunits) was significantly

more dynamic/accessible upon replacement of β1/2/5 by the immuno-subunits (**Fig. 4D** red circles, **Fig. S4-S5**). This suggests a long range mechanism enabling the pore of the i20S to dwell longer in the open-state, and could explain its generally higher activity[44]. On the contrary, three regions located on the solvent-accessible interface of the α-ring were significantly more dynamic/accessible in the std20S than in the i20S, namely the C-ter part of α3 (238-261), the 165-178 stretch of α1 and the 167-181 stretch of α5 (**Fig. 4D**, **Fig. S2**, **Fig. S5**). These amino-acid stretches constitute potential binding sites for the proteasome regulators, so their dynamics change could explain the preferential association of specific regulators to different subtypes of the 20S. Interestingly, these three subunits also contain regions that are more accessible in the std20S on the β-ring facing interface (**Fig. 4C**), suggesting that this dynamic behavior can be related to the presence of the standard catalytic subunits within the β-ring. More precisely, the 102-114 and 146-152 stretches of α1, which were more deuterated in the std20S compared to the i20S, are in direct contact with a portion of β2/β2i (69-72) that was also more accessible in the std20S (**Fig. S4**). Altogether, these results confirm the "inner-to-outer" ring allosteric effect occurring upon incorporation of the immuno β subunits that lead to an α-ring that was more dynamic near the pore entry but presented less accessible anchor regions on the outside, especially the C-ter of α3.

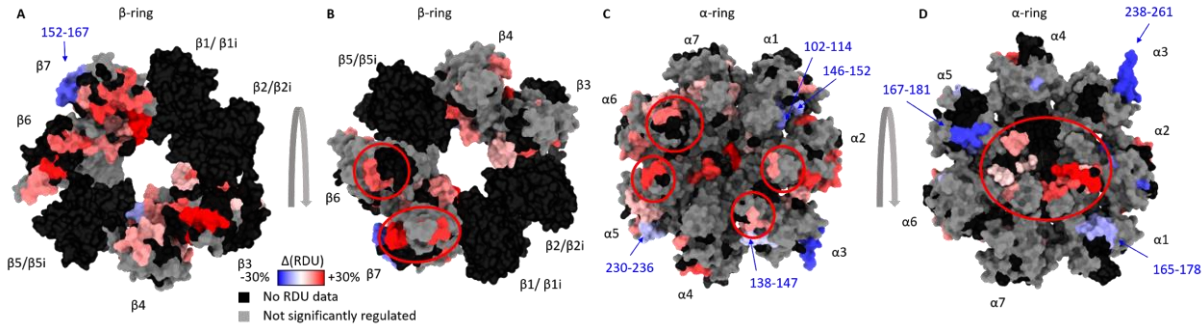

Figure 4. Differential analysis of std20S and i20S. (A-D) Sum of differential relative uptakes (ΔRDU) between the i20S and the std20S: β-ring/β-ring interface **(A)**; β-ring facing the α-ring (**B)**; α-ring facing the β-ring **(C)**; solvent-facing α-ring **(D)**. Color coded regions are significantly more accessible/dynamic in the std20S (blue=-30%) or i20S (red=+30%) and regions of interest are circled or annotated with the same colors. Regions that are not covered in one or both conditions, or do not pass the statistical threshold are represented in black and grey, respectively. "RDU": relative deuterium uptake.

The comparative analysis of the PA28 regulators indicate a less dynamic activation loop in PA28β

There is no structure yet for PA28γ but those of the human homo-heptameric PA28α (non-physiological) and murine hetero-heptameric $PA28\alpha_4\beta_3$ were resolved in 1997[27] and 2017[28], respectively. In both cases, the monomers are composed of a four-helix bundle, assembled as a barrel-shaped heptamer (**Fig. 5**) that controls proteasome catalytic activity through a conserved activation loop[45,46]. The structures of PA28α, PA28β and PA28αβ miss a region of 15 to 31 residues bridging the α-helices 1 and 2, although they were present in the recombinant constructs (**Fig. 5A** and **Fig. S7** in red). These loops, most likely flexible, should sit on top of the heptameric donut-shape regulator and might thereby control the substrate access to the proteasome. The human PA28γ chain has a similar loop that is even longer (35 residues: I69 to M103), and no structural information on this missing region has ever been reported, to our knowledge, for both human regulators. Since the sequence identity of human PA28γ is closer to PA28α (40%) than PA28β (35%) or PfPA28 (34%) (**Table S5**), we generated a homology model of human PA28γ (**Fig. 5D**) using the structure of human PA28α (PDB:1AV0) as a template with the SWISS-MODEL server[47].

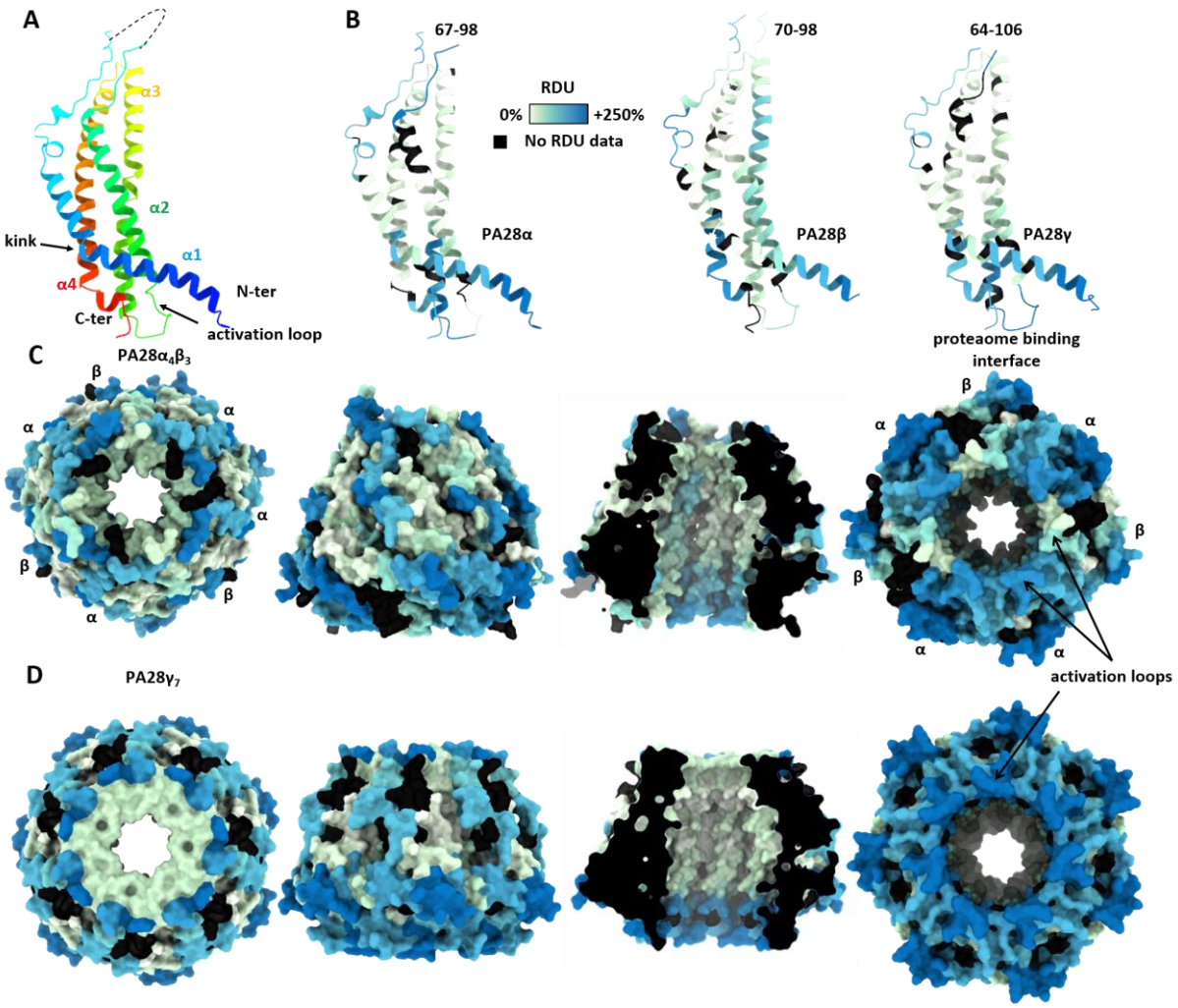

Figure 5. PA28 regulators present flexible loops on both ends of the channel. (A-B) Structure of monomeric PA28α showing the 4-helix-bundle colored based on amino-acid numbering **(A)** or sum of hydrogen-deuterium relative uptake accumulated over 30 min **(B). (C-D)** Surface accessibility of the heptameric complexes PA28$\alpha_4\beta_3$ **(C)** and PA28γ_7 **(D)** viewed from the top (left), front and inside (middle), and bottom (right). Regions that were not detected are represented in black. "RDU": relative deuterium uptake.

The sequence coverages obtained upon pepsin digestion were above 90% for all three PA28 subunits across all conditions (**Fig. 5**, **Fig. S1, Fig. S6-7** and **Table S1**). A first look at the deuteration pattern revealed similar dynamics for both PA28αβ and PA28γ receptors with a very strong protection of most residues inside the channel (**Fig. 5C-D**, middle and **Fig. S7**). The missing loops (**Fig. S7** in red) were very quickly deuterated, a sign of high accessibility/flexibility, that could explain their absence in known structures. The proteasome-facing interface (essentially composed of the unstructured N- and C-termini and the activation loops) (**Fig. 5C-D**, right) and the outside entrance of the channel (**Fig. 5C-D**, left) were also strongly deuterated. Remarkably, the regions involved in the binding (C-ter) and activation (activation loops) of the proteasome were very accessible/dynamic when both regulators were alone in solution. However, the activation loop was less deuterated in PA28β.

PA28γ and PA28αβ deuteration profiles suggest an allosteric change upon association with the 20S proteasome, involving the activation loops and a kink in the 1st α-helix

We compared the deuteration rates of the PA28 regulators alone and in complex with the std20S. As expected, the regions of the proteasome-facing interface became highly protected in the complex

compared to the regulators alone (**Fig. 6** right, in blue; **Fig. S6**, **Fig. S8-S9**). The activation loops, located at the binding interface with the 20S, and known to interact with the N-ter of the α subunits of the 20S to open its central pore, were highly dynamic/accessible in both PA28 analysed alone (**Fig. 5C-D** right**,** and **Fig. S6-S7**). Our data show that binding of PA28αβ to the std20S strongly protected the activation loops as well as their neighbouring residues (136-147, 153-159 and 232-249 in PA28α; 123-134, 140-145 and 215-221 in PA28β, **Fig. 6A** and **Fig. S8-S9**). The fact that PA28β activation loop was found less dynamic (**Fig. 5C**) and less protected upon 20S binding (**Fig. 6A**) compared to PA28α suggests that they might play different but complementary roles in the activation of the 20S. The protection of PA28γ activation loop (region 146-152) upon binding to the std20S (**Table S4**, sum of differences of RDU across time points = -0.20; corrected p-value = 1.5E-8 for peptide 145-152 of PA28γ) was also statistically significant but notably less pronounced than what observed in PA28αβ (**Fig. 6B** and **Table S4**, sum of differences of RDU across time points = 0.83; corrected p-value = 1.1E-17 for peptide 136-147 of PA28α), which could indicate that the std20S has a greater affinity for PA28αβ than for PA28γ.

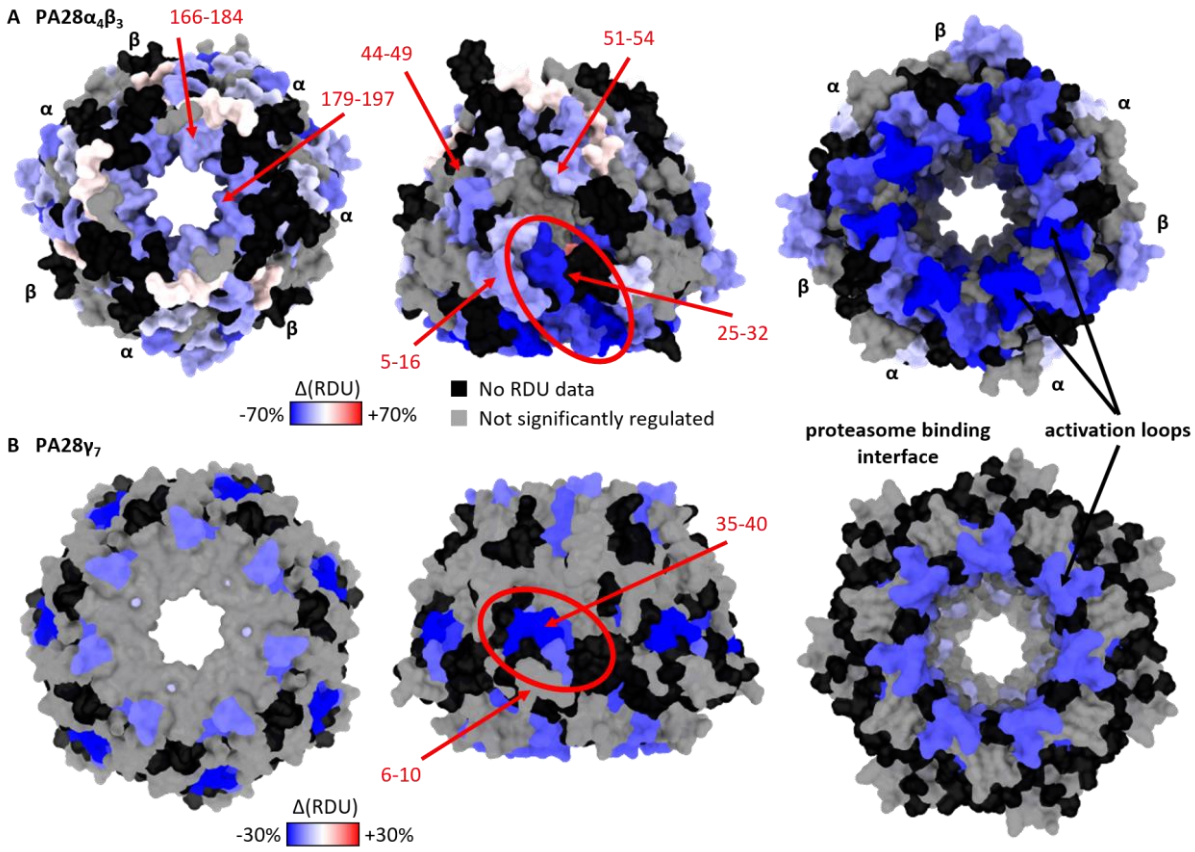

Figure 6. Activation of PA28αβ and PA28γ by the std20S involves a rearrangement of the N-ter kink and an allosteric change. Residues of PA28αβ **(A)** and PA28γ **(B)** that are statistically protected/less dynamic upon binding of the std20S proteasome are located around the N-ter kink (red ovals), the activation loop and 20S interface (arrows) and the entry of the channel (left). The sum of differential relative uptakes accumulated over 30 min deuteration of the PA28 regulators with and without the std20S proteasome is color coded from -70% (blue) to +70% (red) for PA28αβ **(A)** and from -30% (blue) to +30% (red) for PA28γ **(B)**. Residues in grey were not considered significantly different according to the statistical thresholds presented in **Fig. 1D**. Residues with no RDU information in one or both conditions are in black. "Δ(RDU)": sum of differences of relative deuterium uptake.

Interestingly, we observed other regions that became less dynamic/accessible upon complex formation. In PA28α (25-32) and PA28γ (35-40), the kinks of the first α-helix (**Fig. 5A** and **Fig. 6**, red

ovals) were strongly protected upon binding to the std20S. We observed that the N-ter region (5-16) of PA28β, that faces the kink in PA28α, was also significantly protected upon interaction with the std20S (**Fig. S8**). We thus hypothesize that this interaction between PA28α and PA28β might be strengthened, and/or structurally rearranged. The N-ter (6-10) of PA28γ facing the kink, was slightly but not significantly protected in our statistical analysis (**Fig. 6B** and **Fig. S8**).

Furthermore, regions located on the opposite side of the heptamer were also found to be protected upon binding with the std20S: the loops between helices 3 and 4 of PA28α (179-197), PA28β (166-184) and PA28γ (191, 203-208) (**Fig. 6**, Lys191 of PA28γ not visible in this view) as well as the unstructured loops following the helix 1 in PA28β (44-49 in PA28α, 51-54 in PA28β, **Fig. 5** and **Fig. 6A**) but also the flexible loop (60-101) of PA28γ that is missing in our structural model (**Fig. 5B**). These regions include the constriction sites at the top of both activators (Lys190 in PA28α, Lys177 in PA28β and Lys191 in PA28γ) that were significantly protected upon binding to the std20S (**Fig. 6** and **Fig. S8**). These changes in dynamics, observed on regions that are located so far away from the binding interface (activation loops and C-ter), show the existence of long-range allosteric motions of PA28 activators upon binding to the 20S.

We then compared the impact of std20S *vs* i20S binding on PA28 solvent accessibility (**Fig. S8**). Most of the reduction in accessibility/flexibility that was observed on the PA28 chains upon binding to the std20S were dampened upon interaction with the i20S. Both the activation loops and C-ter parts of PA28αβ were more protected upon interaction with the std20S compared to the i20S suggesting that the interaction is stronger with the std20S than the i20S. Concerning PA28γ, its activation loop (region 146-152), kink (35-40) and missing loop (60-101) were also significantly more protected upon interaction with the std20S (**Fig. S8**).

Our HDX-MS data thus indicate that PA28αβ strongly interacts with the std20S, thereby forming an interface highly protected from deuteration, and that this protection extends to the kinks of the first α-helices (at the interface between PA28α and PA28β) and up to the flexible loops on the other side of the regulator. The deuteration profile of PA28γ in complex with the std20S was similar, with a protection of the binding interface (restricted to the activation loops), of the kinks and of the long loops that are absent from all the homologous X-ray/Cryo-EM structures.

An outer-to-inner allosteric change of the 20S proteasome upon binding to PA28

Atomic force spectroscopy showed that the 20S can alternate between an open and closed state, possibly through allosteric regulation[40,41]. Our HDX-MS data indicate that PA28αβ and PA28γ do not present exactly the same conformational rearrangements upon binding to the 20S, one can thus imagine that their binding might differently and allosterically affect the 20S pore entrance and/or its catalytic sites in an "outer-to-inner" mechanism, as suggested recently[21].

We addressed this question through the comparison of differential deuterium uptake on the whole 20S proteasome in the presence or absence of PA28αβ or PA28γ (**Fig. 7, Fig. S10-S12**). Strikingly, very few regions of the top of the α-ring (in contact with the regulators) were significantly protected in the std20S upon interaction with PA28αβ or PA28γ, and none in the i20S. The same C-ter region of α3 that was found to be more accessible in the std20S compared to the i20S (238-261; see **Fig. 4D**) was protected in the std20S upon interaction with PA28αβ, and to a lesser extent with PA28γ (**Fig. 7A-B**). Other regions of the std20S that were protected when binding PA28αβ include the residues 45-55/78-82 from α4 and 31-37/168-181 from α5 that form two patches on the same solvent-exposed interface (**Fig. 7A**). These three regions seem to form the main anchorage sites of PA28αβ at the surface of the std20S. The rest of the std20S solvent-exposed surface is globally more dynamic upon PA28αβ binding, especially near the pore entrance (N-ter of α1/2/4/5/7) (**Fig. 7A**), which can be interpreted as an

opening of the pore. Another external patch at the interface between α1 (179-191) and α2 (196-202) was also more dynamic upon binding of PA28αβ (**Fig. 7A**).

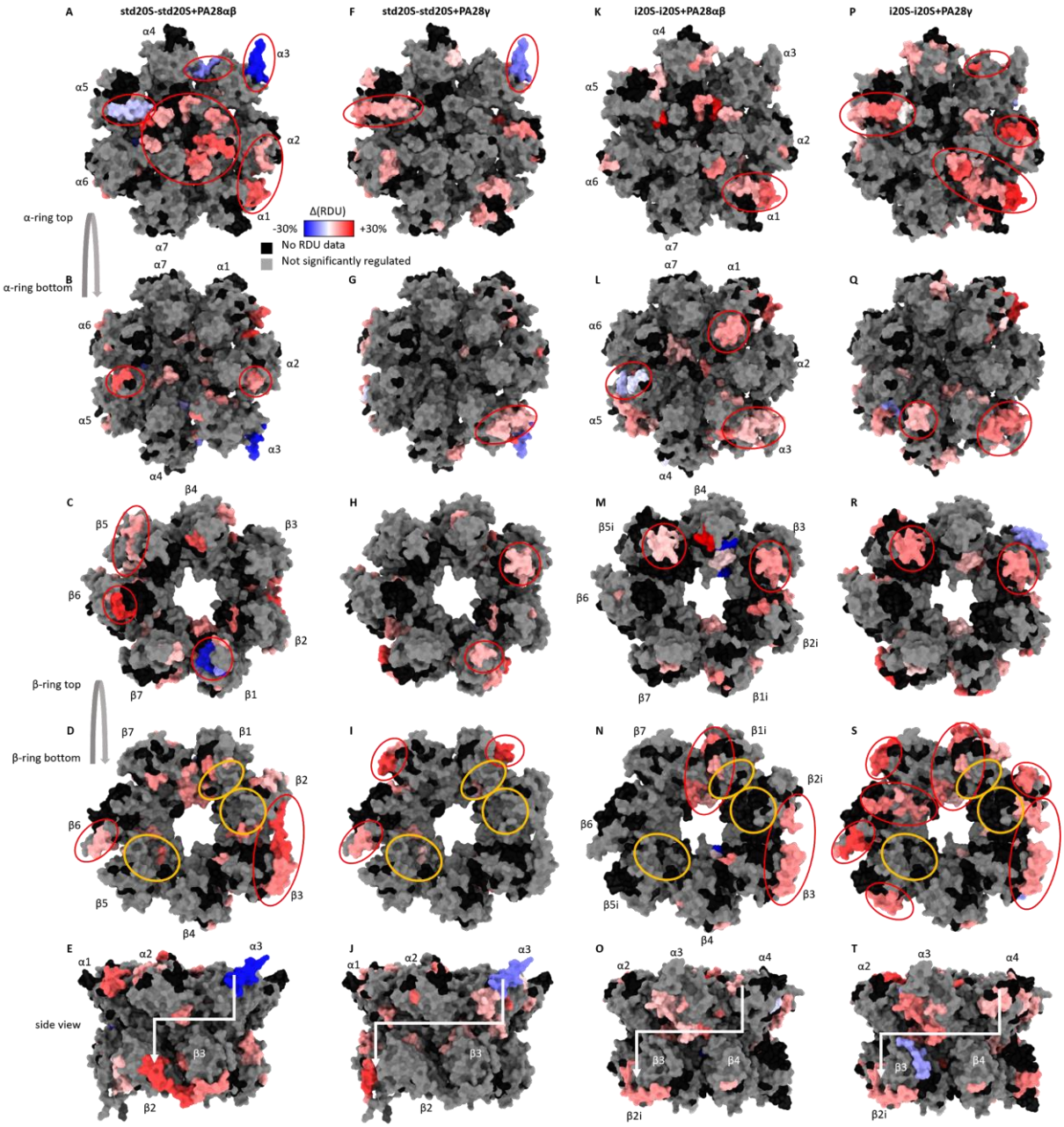

Figure 7. Catalytic-subunit- and regulator-specificity of the outer to inner allosteric changes. Differential relative uptakes accumulated over 30 min deuteration of the 20S proteasomes with and without the PA28 regulators. The regions that were statistically protected or more dynamic upon regulator binding are represented in blue and red, respectively, for the std20S (PDB 5LE5) and PA28αβ (PDB 5MX5) **(A-E)**, the std20S and PA28γ **(F-J),** the i20S (PDB 6E5B) and PA28αβ **(K-O)** and the i20S and PA28γ **(P-T).** Active sites at the β-ring/β-ring interface are circled in orange. The side views of the hemi-proteasome (**J/O/T/E**) show the α-ring and β-ring interface. Residues in grey were not considered significantly different according to the statistical thresholds presented in **Fig. 1D**. Residues with no RDU information in one or both conditions are in black. "Δ(RDU)": sum of differences of relative deuterium uptake.

On the bottom side of the α-ring, the binding of PA28αβ mainly destabilized the 135-145 region of α2 and the α5 bulge (102-107) both located at the interface with the β-ring (**Fig. 7B**, red circles). Interestingly, the α5 bulge (**Fig. 7B**) faces the 109-135 stretch of β6 that encompasses 4 peptides found

to be more deuterated upon PA28αβ binding and is in close vicinity to the interface with β5 that also became more dynamic (**Fig. 7C,** red circles). Although not close enough to make hydrogen bonds, the 135-145 region of α2 (**Fig. 7B**) faces the β2/β3 interface that was found more flexible/accessible upon PA28αβ binding, especially in the 186-202 C-ter region of β2 that extends to reach out to β3 (**Fig. 7D**, circled in red). The only peptides of the β-ring that were found less dynamic upon PA28αβ binding are located on β1 (72-82/122-125/156-159; **Fig. 7C**, circled in red).

Comparing the effect of PA28αβ binding to the std20S (**Fig. 7A-E**) with the other conditions (**Fig. 7F-T**) is not straightforward but we could make the following observations. Although, the destabilization of the N-termini of the α-ring by PA28αβ is almost complete with the std20S (except α7) (**Fig. 7A**), it is restricted to α1/α3/α4/α5 with the i20S (**Fig. 7K**), suggesting a partial opening of the pore in this case. Binding of PA28γ affects none of the α subunit N-termini of the std20S (**Fig. 7F**) and only the subunits α2 and α3 N-termini of the i20S (**Fig. 7P**) indicating a less drastic effect of PAγ on the pore opening.

The C-ter part of α3 is involved in the binding or stabilization of PA28 activators in the std20S but not the i20S (**Fig. 7A,F,K,P**). Overall, PA28 binding to the 20S proteasomes globally increased deuterium uptake, especially at the pore entrance, at the α1/α2 interface (**Fig. 7A,F,K,P**), and the β2 C-ter arm that extends towards β3 (**Fig. 7D,E,N,O,S,T**). Despite these similarities, the dynamics of the std and i20S proteasomes were differently affected depending on their binding partner, suggesting subtle differences in the allosteric motion triggered by their association with the different regulators, as suggested by Toste Rêgo *et al*[21]. PA28γ also protected the α3 C-ter of the std20S (**Fig. 7F**), which seems to induce its destabilization, propagated via α2 (101-119, **Fig. 7F**), β3 (74-86) and β1 (64-70) bulges (**Fig. 7H,** red circles), down to the outer β-ring/β-ring interface of β1 (178-205), β6 (151-159) and β7 (152-167) (**Fig. 7I,** red circles). As mentioned earlier, the C-ter of α3 in the i20S was not significantly affected by the association of the i20S with PA28 regulators according to our statistical thresholds (**Fig. 7K,P**). In both cases, we observed a remodelling of the α-ring that propagated to the β-ring via the α1/β3/β5i bulges for PA28αβ (**Fig. 7L,M**) and via the α4/β3/β5i bulges for PA28γ (**Fig. 7Q,R**). The regions of the β-ring/β-ring interface eventually affected include β2i and β1i with PA28αβ (**Fig. 7N**) and β2i/β1i/β5i/β6 with PA28γ (**Fig. 7S**).

The sequence coverage was limited around the catalytic sites, which prevented us from drawing exhaustive conclusions on the differential impact of regulator/20S complex formation on the proteasome active sites. However, the active sites of β1 (10-25), β2 (16-42) and β5 (29-36) were partially but significantly more dynamics/accessible upon PA28αβ binding (**Fig. 7D**, orange circles), in line with an increased proteolytic activity. Binding of PA28αβ also increased the solvent accessibility of β1i active site (10-17) (**Fig. 7N**); in good agreement with previous work showing that the caspase-like activity of the i20S was enhanced to a higher extent by PA28αβ[48]. PA28γ was reported to have little or no effect on the i20S[49], whereas it is known to increase all three std20S activities[50]. Our data does not indicate any major change in solvent accessibility of the std20S active site upon interaction with the regulator (**Fig. 7I**). However, it revealed a significant decrease of the solvent accessibility of β2i N-ter (2-6) upon interaction with PA28γ (**Fig. S11).** Thus, the catalytic regulation observed upon PA28γ binding to the std20S may be driven by changes occurring further away from the active site.

Discussion

This work provides the first data set of structural information on the human i20S compared to the std20S alone or bound to both PA28 regulators. It rationalizes from a mechanistic point of view the previous observations that replacement[44], modification[29] or ligand binding[44,51] to the catalytic subunits can allosterically modify the structure of the 20S core particle and alter its binding surface with potential PIPs. A main advantage of HDX-MS is that information can also be retrieved from very flexible

loops, unlike X-ray crystallography or cryo-EM. Another advantage is that it is not theoretically limited by the size of the complex since the proteins are digested into peptides after deuteration: it can be applied to very small proteins (unlike cryo-EM) or very large complexes (unlike NMR). Large oligomeric complexes containing a reduced number of different monomers (thereby limiting the number of chemical shifts) have already been analyzed by NMR, such as the prokaryotic 20S proteasome from *Thermoplasma acidophilum* constituted of 14 identical α and 14 identical β subunits[29]. With the recent exception of the DNA-PKc analysis[52] (1 monomer of 469 kDa) that required a home-made dedicated ion-source, HDX-MS is usually performed either on rather small and simple systems[53] or on very large homo-oligomeric complexes[54,55], due to some technical limitations in protein digestion, peptide separation and data analysis. In comparison, our study of the 20S proteasome bound to PA28αβ encompasses 16 different ~25 kDa monomers. Despite this analytical challenge, we obtained an average sequence coverage per subunit of 89% for the 20S alone and 81% when in complex with PA28 regulators. The thorough statistical analysis of these data provide a wealth of information on the proteasome dynamics, binding interfaces and allosteric changes upon incorporation of the immuno subunits or activation by the PA28 regulators. The major findings of this project are summarised in **Fig. 8**.

Our conformational maps revealed the subtle rearrangement of the C-ter of α3 , more precisely the residues 238-261 were less dynamic/accessible upon incorporation of the immuno catalytic subunits (in purple **Fig. 8A**). This was suggested before in the work of Arciniega *et al*, where the authors compared all the 20S high-resolution structures available in the Protein Data Bank (PDB) in 2014 (46 structures from yeast, 4 murine and 1 bovine)[44]. In this work, the 220-230 stretch of α3 also presented conformational changes upon ligand binding to the β5 subunit in yeast. The principal component analysis (PCA) of these 56 crystal structures revealed that the mouse std20S and i20S clustered with the yeast apo and peptide-bound forms, respectively. This suggests that the allosteric change occurring on the C-ter part of the α3 subunit upon ligand binding to β5 in the yeast 20S could be similar to the change in solvent accessibility/dynamics that we observed between the std20S and the i20S conformational maps. The C-ter of α3 is a highly charged region pointing towards the outer surface of the α-ring that has also been suggested to be the binding site for the Insulin-Degrading-Enzyme[56]. It could be involved in the binding of PA28αβ and PA28γ to the std20S, or in its subsequent activation. Interestingly, the very end of the C-ter of α3 is absent from most structures of the human 20S proteasome, which confirms its high flexibility but also impedes any modeling of the interaction with PA28 regulators. We checked whether the C-ter of α3 was involved in the interaction between the 20S and PA28 regulator in the *Plasmodium falciparum* cryo-EM structure (uniprot entry Q8IDG2)[31], however this protruding C-ter α helix is not present since *P. falciparum* α3 is 9 residues shorter than its human counterpart. It could be characteristic of more evolved 20S proteasomes, and tune their binding with different regulators.

The central pore of the 20S, on the other hand, was more flexible in the i20S compared to the std20S (**Fig. 5D** and in orange **Fig. 8A**). Similarly, the β-facing interface of the α-ring was more dynamic in the i20S than the std20s, and especially α5 that directly faces the β5 (std20S) or β5i (i20S) catalytic subunit (**Fig. 5C**). We propose that the difference of dynamics between the two proteasomes observed at the catalytic sites could be transduced from the inner β-ring to the outer α-ring via α5 and lead to the conformational differences observed on their α3 C-ter (orange arrows **Fig. 8A**). Although HDX-MS does not allow a thorough comparison of the standard and immuno catalytic subunits since their sequences are different, our data set suggests that the substrate pockets S1/S2 of β1 as well as the active site and S1 pocket of β5 are more dynamic than in their immuno-subunit counterparts. It has been shown that β1 PGPH activity is higher than the one of β1i and β5i chymotrypsin activity is higher than the one of β5[57]. This tells us that we cannot directly correlate the substrate pocket flexibility/accessibility with the

level of activity. The slower deuterium exchange observed in the S1 pocket of β5i is in good agreement with the higher number of van der Waals interactions observed in mice[26] and with the specific hydrogen bond that stabilizes the tetrahedral transition state during catalysis of β5i. β2i trypsin activity is higher than the one of β2[57], unfortunately, the sequence coverage of β2 and β2i in our data set does not allow us to see whether their active sites and substrate pockets present different solvent accessibilities.

More interesting is the complementary finding that upon binding of any regulator to the 20S, we observed a similar destabilization of the region of α5 that faces β5/β5i, suggesting that the exact opposite mechanism (from the outer α-ring to the inner β-ring) can also take place when the 20S interacts with PA28 regulators, as suggested earlier by NMR[29].

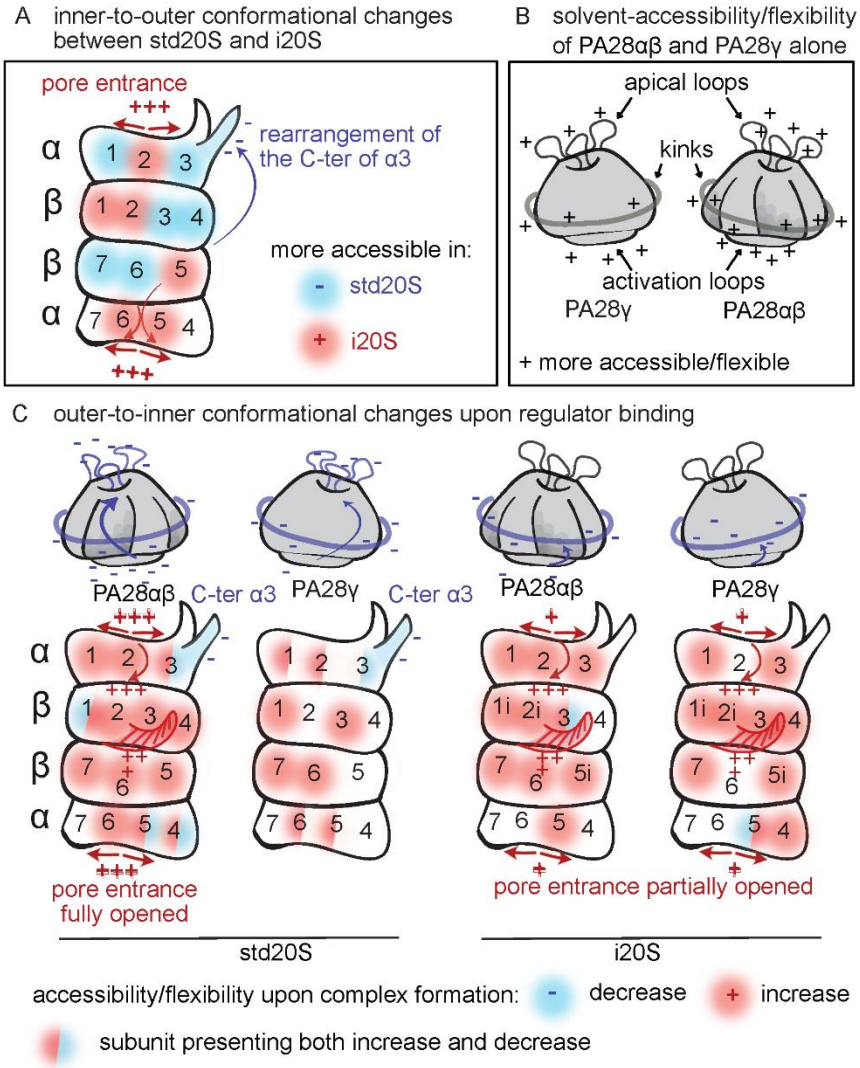

Figure 8. Schematic representation of our major finding. Comparison of std20S *vs* i20S deuteration **(A)** confirms the inner-to-outer allosteric change. While both PA28 show similarities in their dynamic regions **(B)**, their binding induces a reverse outer-to-inner perturbation that depends on both 20S and PA28 subtypes **(C)**.

Overall, our HDX-MS data on the PA28 regulators indicate a general mechanism of activation by the 20S core proteasome. More precisely, the binding of the activation loops and C-ter of PA28 to the 20S seems to trigger a long-range allosteric change at the top of the regulator (loops between helices 1/2 and/or 3/4) via a rearrangement of the N-ter kink of PA28α and PA28γ (**Fig. 8B**). The poorly structured region at the end of helix 1 and before the first missing loop presumably acts as a hinge to convey the

allosteric change from the kink to the top of the regulator. Although present in the three PA28 subtypes, the protection of the activation loop was stronger in PA28α and PA28γ compared to PA28β; most probably explaining why "the affinity of the proteasome towards the PA28αβ complex is about two orders of magnitude higher than towards the homomeric PA28α and PA28β complexes"[58]. Indeed, several studies showed that both PA28α and PA28β were required for an optimum activation of the 20S by PA28αβ[27,28]. We recently showed that PIP30/FAM192A interacts with PA28γ and increases its association with the 20S by a 2-fold factor[50]. It would be interesting to investigate by HDX-MS if the interaction of PIP30/FAM192A with PA28γ allosterically alters its 20S binding surface.

We also provide crucial information on the loops located between helices 1/2 that are missing in every high-resolution structure or model of PA28 homologues, including the recently released crystal structure of the PA28 regulator from *P. falciparum* (PfPA28)[20]. However, small-Angle X-Ray scattering (SAXS) analysis enabled to model them, and showed that these surround the pore[20]. Our HDX-MS data show that these flexible loops sitting on top of PA28, together with the constriction site (conserved Lys between alpha helices 3 and 4) are allosterically stabilized upon binding of the std20S but not the i20S proteasome (**Fig. 8B**). Since these loops are located at the entrance/exit of the activator, any change in flexibility could very well induce changes regarding the nature of both substrates and/or products of the proteasome complex. The loop of PA28α was for example shown to act as a gatekeeper that helps constrain substrates within the catalytic chamber in order to generate shorter peptides[59]. The relative stabilisation of these loops could explain how the binding of different PA28 to different 20S subtypes alters the length/nature of the generated peptides.

Our data also support another hypothesis in which PA28 might modify the 20S products by inducing conformational changes in the proteasomal active sites. Indeed, our results show distinctive changes in dynamics that were detected down to the β-ring and around the catalytic site and/or substrate pockets upon regulator binding (**Fig. 8C**). The general increase in deuteration observed inside the proteolytic channel can of course be partially due to the opening of the pore by the regulators. This is one of the limitations of the technique: one cannot discriminate if an increased deuteration rate is due to an increase in solvent accessibility or in dynamics/flexibility of the residues. However, the fact that regions on the outside of the 20S were also more dynamic upon PA28 binding (**Fig. 7**), strongly suggests that the effects observed inside the cavity are not only due to the opening of the pore.

Our data set shows a stronger protection of PA28αβ than PA28γ when these bind the std20S (**Fig. 6** and **Fig 8B**). Globally, both PA28 were more protected upon interaction with the std20S than with the i20S (**Fig. S8-S9**). This was mirrored by the presence of regions on the α-ring of the i20S that were less protected than in the std20S upon incubation with both PA28, whereas previous studies showed that the interaction of PA28αβ was stronger with the i20S than with the std20S[60] or equivalent[17]. We thus think that the protection cannot be directly correlated to relative binding affinities, especially because we monitor deuteration on protein complexes at steady-state (after 30 min incubation).

Although not similarly distributed, the global level of destabilization observed on the core proteasomes was similar in all four conditions tested (**Fig. 7**). It seems more interesting here to focus on the comparison of the regions undergoing the most structural rearrangements. We thus observed that each pair of PA28/20S complex underwent long-range conformational rearrangements in specific regions (**Fig. 8C**), confirming the recent assertion from Toste Rêgo and Da Fonseca[21] according to which ''although the detailed molecular basis of allosteric modulation of the proteasome active sites has not yet been described for any other proteasome, regulator related effects should be expected because it is known that different proteasome regulators induce different effects on each of the three proteasome proteolytic activities.'' In accordance with this statement, we found that different subunit α N-termini were destabilized depending on the PA28/20S pair (in red **Fig.8C**), suggesting different

levels of opening of the central pore. The β2 C-ter extending towards β3 was destabilized in all the conditions, except when the std20S was activated by PA28γ. On the contrary, the region just before the α3 C-ter (217-236) was protected upon PA28 binding in all cases, except when the std20S bound PA28αβ. Interestingly, this stretch is in close vicinity to the 74-86 region of β3, which was also protected in all conditions tested except std20S/PA28αβ. These observations could provide a basis to understand how regulator binding could propagate from the α- to the β-ring depending on the activator/20S pair.

Altogether, this data set gathers a wealth of information on the allosteric activation of the 20S proteasome complexes that will most surely be confirmed by upcoming structural and functional studies. This work sets the basis for the use of HDX-MS as a new tool to investigate dynamic events on megadalton assemblies such as the proteasome, and we foresee its application to other big complexes including ribosomal particles, inflammasomes, nucleosomes, to name a few. Concerning the proteasome complexes, we think that this method could be applied to characterize, not only the binding sites of many new proteasome inhibitors, but also to identify their potential allosteric effects on the 20S core complex. The same is true for the many PIPs that regulate proteasome function and are still poorly characterized from a structural point of view[61].

Material and Methods

Reagents

Unless stated otherwise, all reagents were purchased from Sigma-Aldrich. The std20S, i20S, PA28γ and PA28αβ were purchased from Enzo Life Science. Deuterium oxide, deuterium chloride and sodium deuteroxide solutions were from Euriso-top.

Automated Hydrogen-Deuterium eXchange coupled to Mass Spectrometry (HDX-MS)

HDX-MS experiments were performed on a Synapt-G2Si (Waters Scientific, Manchester, UK) coupled to a Twin HTS PAL dispensing and labelling robot (LEAP Technologies, Carborro, NC, USA) via a NanoAcquity system with HDX technology (Waters, Manchester, UK). Each step was optimized to minimize sample loss and work with such a heterogeneous and diluted sample:

- Method in HDxDirector:

The method recommended by Waters (HDX System Suitability Test) injects only 25% of the sample that is aspirated from the protein vial. In order to reduce sample loss, we 1) used a sample loop of 100 µl instead of 50 µl, 2) carefully reduced all the dead volumes and 3) used a stronger acid (500 mM glycine pH 2.3 instead of 50 mM K_2HPO_4, 50 mM KH_2PO_4, pH 2.3) in order to optimize the ratio of quenching volume (10% instead of 50%). With this workflow, we increased by more than threefold the amount of starting material injected (79%). 20S proteasomes were incubated alone or with a 2-fold molar excess of PA28, with final concentrations of 0.4 µM and 0.8 µM, respectively. 5.7 µL of protein were aspirated and 5.2 µL were diluted in 98.8 µL of protonated (peptide mapping) or deuterated buffer (20 mM Tris pH/pD 7.4, 1 mM EDTA, 1 mM DTT) and incubated at 20 °C for 0, 0.5, 1, 5, 10 and 30 min. 99 µL were then transferred to vials containing 11 µL of pre-cooled quenching solution (500 mM glycine at pH 2.3). For experiments involving PA28αβ, the quenching buffer was supplemented with 250 mM tris-(2-carboxyethyl) phosphine (TCEP) in order to reduce the disulphide bridge between Cys21 of chain α and Cys3 of chain β. After 30 sec. of quenching, 105 µL were injected into a 100 µL loop. Proteins were digested on-line with a 2.1 mm x 30 mm Poros Immobilized Pepsin column (Life Technologies/Applied Biosystems, Carlsbad, CA, USA). The temperature of the digestion room was set at 15°C.

- Chromatographic run

In order to cope with the unusual sample heterogeneity, the runtime of the chromatographic separation (12 min) was doubled compared to the one used for smaller protein complexes (6 min). Peptides were desalted for 3 min on a C18 pre-column (Acquity UPLC BEH 1.7 µm, VANGUARD) and separated on a C18 column (Acquity UPLC BEH 1.7 µm, 1.0 x 100 mm) by the following gradient: 5% to 35% buffer B (100% acetonitrile , 0.2% formic acid) for 12 min, 35% to 40% for 1 min, 40% to 95% for 1 min, 2 min at 95% followed by 2 cycles of 5% to 95% for 2 min and a final equilibration at 5% buffer A (5% acetonitrile, 0.2% formic acid) for 2min. The total runtime was 25 min. The temperature of the chromatographic module was set at 4°C. Experiments were run in triplicates and the protonated buffer was injected between each triplicate to wash the column and avoid cross-over contamination.

- MS acquisition

The acquisitions were performed in positive and resolution mode in the m/z range 50 to 2000 Th. The sample cone and capillary voltages were set at 30 V and 3 kV, respectively. The analysis cycles for non-deuterated samples alternated between a 0.3 sec low energy scan (Trap and Transfer collision energies set to 4 V and 2 V, respectively), a 0.3 sec high energy scan (Ramp Trap and Transfer collision energies set to 18 V to 40 V and 2 V to 2 V, respectively) and a 0.3 sec lockspray scan (0.1 µM [Glu1]-Fibrinopeptide in 50% acetonitrile, 50% water and 0.2% formic acid infused at 10 µL/min). The lockspray trap collision energy was set at 32 V and a GFP scan of 0.3 sec is acquired every min. In order to double the signal intensity of deuterated peptides, deuterated samples were acquired only with the low energy and lockspray functions.

- Data analysis

Peptide identification was performed with ProteinLynx Global SERVER (PLGS, Waters, Manchester, UK) based on the MS^E data acquired on the non-deuterated samples. The MSMS spectra were searched against a home-made database containing sequences from the 17 std20S and i20S subunits, PA28α, PA28β, PA28γ and pepsin from *Sus scrofa*. Peptides were filtered in DynamX 3.0 with the following parameters: peptides identified in at least 2 replicates, 0.2 fragments per amino-acid, intensity threshold 1000. The quantitative analysis of deuteration kinetics was performed using the statistical package R (R Development Core Team, 2012; http://www.R-project.org/) on the corresponding MS intensities. The deuterium uptakes of each ion for each time point were calculated based on the theoretical maximum, considering that all amino-acids (except proline residues and the first amino-acid or each peptide) were deuterated, and then averaged (weight = intensity) to get a value of relative deuterium uptake (RDU) per peptide sequence/condition/time point (see **Fig. S2, S6, S10** and **Table S2,S6**). To identify the protein regions that presented conformational changes in complex vs. alone, we performed an ANOVA (Anova(), type = "III", singular.ok = T) followed by Benjamini Hochberg correction of the *P*-value. For each comparison, we considered significantly regulated the peptides with a corrected *P*-value ≤ 0.01 and an absolute difference of RDU above 0.01569 (4 times the mean absolute difference of RDU in the entire data set) for 3 successive time points (**Table S4**). The corresponding volcano plots are presented in **Fig. S5, S9, S12** and all the regions statistically regulated in all the differential HDX-MS analysis are listed in **Table S3**. The RDU and differences of RDU (for protein alones or comparison between conditions, respectively) were consolidated using the values of the smallest peptide to increase the spatial resolution (see consolidation heatmaps in **Fig. S3, S4, S7, S8, S11**). These data (per time point or sum of all time points) were then used for structural data mining with the recently developed open-source web application called HDX-Viewer[39] that allows to directly plot and visualize the whole data set (14 different subunits per proteasome core particle) on the proteasome 3D structure. The scripts corresponding to the quality control and statistical analysis of

this data set are available at zenodo.org with the DOI 10.5281/zenodo.3769174 under the Creative Commons Attribution 4.0 International licence. All molecular representations were generated in UCSF ChimeraX version: 0.9 (2019-06-06)[62].

Modeling:

The PA28γ model was generated using the structure of human PA28α (PDB:1AV0) as a template with the SWISS-MODEL server[47]. This model misses the first 3 and the last 7 amino-acids, as well as the 64-106 stretch.

Data availability

The R scripts of the analysis, with the fasta files and output tables and cxc files are freely available at zenodo.org with the DOI 10.5281/zenodo.3769174 under the Creative Commons Attribution 4.0 International licence.

The mass spectrometry proteomics data have been deposited to the ProteomeXchange Consortium via the PRIDE[63] partner repository with the data set identifier PXD018921.

Supplementary Information

Figure S1. Sequence coverage and number of peptides obtained upon pepsin digestion of the 20S and PA28 subunits. The bars present the sequence coverage (top) and number of peptides (bottom) obtained for each subunit in the samples with the proteins alone (black) or in complex (grey).

Figure S2. Deuteration uptake curves obtained for each peptide of each subunit of the std20S and i20S. Each plot corresponds to a single peptide. Its sequence, mass and location in the protein sequence (start - stop) are indicated in the plot titles. Points are the RDU of each replicate, lines are their mean. These data can be found in **Table S2**.

Figure S3. Deuteration heatmaps of each α and β subunits of the 20S subunits, alongside their peptide sequence. Relative deuterium uptakes between 0.5 and 30 min color-coded from 0% (white) to 60% (blue). Non-detected regions are colored in black. The solid lines correspond to the peptides from which the RDU values were reported in the consolidated data, the dashed lines correspond to portions of peptides that were not reported because the same sequence portion was covered by a shorter peptide. This representation is explained in **Fig. 1B**.

Figure S4. Differential deuteration heatmaps of each α and β subunits of the std20S *vs.* i20S. Differential relative uptakes between the i20S and the std20S from 0.5 to 30 min color coded from -10% (blue, more flexible/dynamic in the i20S) to +10% (red, more flexible/dynamic in the std20S). Non-detected regions are colored in black. Peptide coverage is represented by lines above the heatmaps. The solid lines correspond to the peptides from which the RDU values were reported in the consolidated data, the dashed lines correspond to portions of peptides that were not reported because the same sequence portion was covered by a shorter peptide. This representation is explained in **Fig. 1B**. Additionally, the peptides that were considered significantly regulated according to the thresholds indicated in **Fig. 1D** are colored in yellow.

Figure S5. Volcano plots showing the peptides significantly different when comparing the deuteration of the std20S *vs.* i20S. Each peptide is plotted in function of its statistical significance (y-axis: -log10(BH-corrected p-value)) and its difference of accessibility in the std20S compared to the

i20s (x-axis: sum of RDU differences across time points). The peptides passing the statistical thresholds presented in **Fid. 1D** are colored: peptides that are statistically more flexible/dynamic in the i20S are represented in blue and those more flexible/dynamic in the std20S in red. These data can be found in **Table S4**.

Figure S6. Deuteration uptake curves obtained for each peptide of PA28α, PA28β and PA28γ alone and in complex with the std20S and i20S. Each plot corresponds to a single peptide. Its sequence, mass and location in the protein sequence (start - stop) are indicated in the plot titles. Points are the RDU of each replicate, lines are their mean. These data can be found in **Tables S2,S6**.

Figure S7. Deuteration heatmaps of PA28α, PA28β and PA28γ alongside their peptide sequence. Relative deuterium uptakes between 0.5 and 30 min color-coded from 0% (white) to 60% (blue). Non-detected regions are colored in black. The solid lines correspond to the peptides from which the RDU values were reported in the consolidated data, the dashed lines correspond to portions of peptides that were not reported because the same sequence portion was covered by a shorter peptide. This representation is explained in **Fig. 1B**. The residues corresponding to the disordered loops located between helices 1/2 and that are missing in every high-resolution structures are highlighted with red rectangles.

Figure S8. Differential deuteration heatmaps of each PA28 subunit alone *vs.* in complex with the std20S or i20S. Differential relative uptakes from 0.5 to 30 min color coded from -30% (blue, less flexible/dynamic in the complex) to +30% (red, more flexible/dynamic in the complex) for PA28αβ and from -10% (blue) to +10% (red) for PA28γ. Peptide coverage is represented by lines above the heatmaps. The solid lines correspond to the peptides from which the RDU values were reported in the consolidated data, the dashed lines correspond to portions of peptides that were not reported because the same sequence portion was covered by a shorter peptide. This representation is explained in **Fig. 1B**. Additionally, the peptides that were considered significantly regulated according to the thresholds indicated in **Fig. 1D** are colored in yellow.

Figure S9. Volcano plots showing the peptides significantly different when comparing the deuteration of the PA28 subunits alone *vs.* in complex with the std20S or i20S. Each peptide is plotted in function of its statistical significance (y-axis: -log10(BH-corrected p-value)) and its difference of accessibility in PA alone or in complex with the 20S (x-axis: sum of RDU differences across time points). The peptides passing the statistical thresholds presented in **Fid. 1D** are colored: peptides that are statistically less flexible/dynamic in the PA28/20S complex are represented in blue and those more flexible/dynamic in the PA28/20S complex in red. These data can be found in **Table S4**.

Figure S10. Deuteration uptake curves obtained for each peptide of each subunit of the std20S and i20S alone or in complex with PA28αβ or PA28γ. Each plot corresponds to a single peptide. Its sequence, mass and location in the protein sequence (start - stop) are indicated in the plot titles. Points are the RDU of each replicate, lines are their mean. These data can be found in **Table S6.**

Figure S11. Differential deuteration heatmaps of each α and β subunits of the std20S and i20S alone *vs.* in complex with PA28αβ or PA28γ. Differential relative uptakes from 0.5 to 30 min color coded from -10% (blue, less flexible/dynamic in the complex) to +10% (red, more flexible/dynamic in the complex). Peptide coverage is represented by lines above the heatmaps. The solid lines correspond to the peptides from which the RDU values were reported in the consolidated data, the dashed lines correspond to portions of peptides that were not reported because the same sequence portion was covered by a shorter peptide. This representation is explained in **Fig. 1B**. Additionally, the peptides that were considered significantly regulated according to the thresholds indicated in **Fig. 1D** are colored in yellow.

Figure S12. Volcano plots showing the peptides significantly different when comparing the deuteration of the std20S and i20S alone or in complex with PA28αβ or PA28γ. Each peptide is plotted in function of its statistical significance (y-axis: -log10(BH-corrected p-value)) and its difference of accessibility in PA alone or in complex with the 20S (x-axis: sum of RDU differences across time points). The peptides passing the statistical thresholds presented in **Fid. 1D** are colored: peptides that are statistically less flexible/dynamic in the PA28/20S complex are represented in blue and those more flexible/dynamic in the PA28/20S complex in red. These data can be found in **Table S4**.

Table S1. Sequence coverage and number of peptides obtained upon pepsin digestion of the 20S and PA28 subunits.

Table S2. Relative deuterium uptakes calculated for each peptide in the data set of the proteins alone.

Table S3. List of all the amino-acid stretches statistically regulated in all the differential HDX-MS analysis

Table S4. Outputs of the statistical analysis.

Table S5. Identity matrix generated by Clustal2.1 showing the percentage of identity between *Pf*PA28 and human PA28α, PA28β and PA28γ.

Table S6. Relative deuterium uptakes calculated for each peptide in the data set of the proteins alone and in complex.

Additional Material (PRIDE repository)

.raw data of each LC-MS(MS) acquisition.

.fasta file used for the MSMS interrogation in PLGS.

IA.csv output files from PLGS used for the sequence coverage of non-deuterated proteins in DynamX.

.CSV output files from our analysis in DanymX used for the kinetic plots (**Fig. S2, S6, S10**).

.pml output files from our analysis in DynamX, to be used with the corresponding .pdb files in HDX-Viewer.

.pdb files of the std20S (5LE5), the i20S (6E5B), PA28αβ (5MX5) and PA28γ (Swiss-Model) used for the 3D analysis in HDX-Viewer with the corresponding .pml files.

.csx sessions for the direct 3D visualization of the deuteration uptakes in ChimeraX.

References

1. Aiken, C. T., Kaake, R. M., Wang, X. & Huang, L. Oxidative Stress-Mediated Regulation of Proteasome Complexes *. *Mol. Cell. Proteomics* 1–11 (2011) doi:10.1074/mcp.M110.006924.
2. Boisvert, F.-M., Lam, Y. W., Lamont, D. & Lamond, A. I. A quantitative proteomics analysis of subcellular proteome localization and changes induced by DNA damage. *Mol. Cell. Proteomics MCP* **9**, 457–470 (2010).
3. Gomes, A. V. Genetics of proteasome diseases. *Scientifica* **2013**, 637629 (2013).
4. Basler, M., Mundt, S., Bitzer, A., Schmidt, C. & Groettrup, M. The immunoproteasome: a novel drug target for autoimmune diseases. *Clin. Exp. Rheumatol.* **33**, S74–79 (2015).
5. Takada, K. *et al.* TCR affinity for thymoproteasome-dependent positively selecting peptides conditions antigen responsiveness in CD8(+) T cells. *Nat. Immunol.* **16**, 1069–1076 (2015).

6. Moscovitz, O. *et al.* A Mutually Inhibitory Feedback Loop between the 20S Proteasome and Its Regulator, NQO1. *Mol. Cell* **47**, 76–86 (2012).
7. Moscovitz, O. *et al.* The Parkinson's-associated protein DJ-1 regulates the 20S proteasome. *Nat. Commun.* **6**, 6609 (2015).
8. Bousquet-Dubouch, M.-P. *et al.* Affinity Purification Strategy to Capture Human Endogenous Proteasome Complexes Diversity and to Identify Proteasome-interacting Proteins. *Mol. Cell. Proteomics* **8**, 1150–1164 (2009).
9. Le Tallec, B. *et al.* 20S proteasome assembly is orchestrated by two distinct pairs of chaperones in yeast and in mammals. *Mol. Cell* **27**, 660–674 (2007).
10. Le Tallec, B., Barrault, M.-B., Guérois, R., Carré, T. & Peyroche, A. Hsm3/S5b participates in the assembly pathway of the 19S regulatory particle of the proteasome. *Mol. Cell* **33**, 389–399 (2009).
11. Xie, Y. Structure, Assembly and Homeostatic Regulation of the 26S Proteasome. *J. Mol. Cell Biol.* **2**, 308–317 (2010).
12. Wang, X. *et al.* The proteasome-interacting Ecm29 protein disassembles the 26S proteasome in response to oxidative stress. *J. Biol. Chem.* **292**, 16310–16320 (2017).
13. Bousquet-Dubouch, M. P., Fabre, B., Monsarrat, B. & Burlet-Schiltz, O. Proteomics to study the diversity and dynamics of proteasome complexes: From fundamentals to the clinic. *Expert Rev. Proteomics* **8**, 459–481 (2011).
14. Weissman, A. M., Shabek, N. & Ciechanover, A. The predator becomes the prey: regulating the ubiquitin system by ubiquitylation and degradation. *Nat. Rev. Mol. Cell Biol.* **12**, 605–620 (2011).
15. Claverol, S., Burlet-Schiltz, O., Girbal-Neuhauser, E., Gairin, J. E. & Monsarrat, B. Mapping and structural dissection of human 20 S proteasome using proteomic approaches. *Mol. Cell. Proteomics MCP* **1**, 567–578 (2002).
16. Arrigo, A.-P., Tanaka, K., Goldberg, A. L. & Welch, W. J. Identity of the 19S 'prosome' particle with the large multifunctional protease complex of mammalian cells (the proteasome). *Nature* **331**, 192–194 (1988).
17. Cascio, P., Call, M., Petre, B. M., Walz, T. & Goldberg, A. L. Properties of the hybrid form of the 26S proteasome containing both 19S and PA28 complexes. *EMBO J.* **21**, 2636–2645 (2002).
18. Ortega, J. *et al.* The Axial Channel of the 20S Proteasome Opens Upon Binding of the PA200 Activator. *J. Mol. Biol.* **346**, 1221–1227 (2005).
19. Huang, X., Luan, B., Wu, J. & Shi, Y. An atomic structure of the human 26S proteasome. *Nat. Struct. Mol. Biol.* **23**, 778–785 (2016).
20. Xie, S. C. *et al.* The structure of the PA28-20S proteasome complex from Plasmodium falciparum and implications for proteostasis. *Nat. Microbiol.* (2019) doi:10.1038/s41564-019-0524-4.
21. Toste Rêgo, A. & da Fonseca, P. C. A. Characterization of Fully Recombinant Human 20S and 20S-PA200 Proteasome Complexes. *Mol. Cell* (2019) doi:10.1016/j.molcel.2019.07.014.
22. Guan, H. *et al.* Cryo-EM structures of the human PA200 and PA200-20S complex reveal regulation of proteasome gate opening and two PA200 apertures. *PLoS Biol.* **18**, (2020).
23. Schweitzer, A. *et al.* Structure of the human 26S proteasome at a resolution of 3.9 \AA. *Proc. Natl. Acad. Sci. U. S. A.* **113**, 7816–7821 (2016).
24. Wehmer, M. *et al.* Structural insights into the functional cycle of the ATPase module of the 26S proteasome. *Proc. Natl. Acad. Sci. U. S. A.* **114**, 1305–1310 (2017).
25. Beck, F. *et al.* Near-atomic resolution structural model of the yeast 26S proteasome. *Proc. Natl. Acad. Sci. U. S. A.* **109**, 14870–14875 (2012).
26. Huber, E. M. *et al.* Immuno- and constitutive proteasome crystal structures reveal differences in substrate and inhibitor specificity. *Cell* **148**, 727–738 (2012).
27. Knowlton, J. R. *et al.* Structure of the proteasome activator REGα (PA28α). *Nature* **390**, 639–643 (1997).
28. Huber, E. M. & Groll, M. The Mammalian Proteasome Activator PA28 Forms an Asymmetric α4β3 Complex. *Structure* **25**, 1473-1480.e3 (2017).

29. Ruschak, A. M. & Kay, L. E. Proteasome allostery as a population shift between interchanging conformers. *Proc. Natl. Acad. Sci. U. S. A.* **109**, E3454–62 (2012).
30. Schrader, J. *et al.* The inhibition mechanism of human 20S proteasomes enables next-generation inhibitor design. *Science* **353**, 594–598 (2016).
31. Ladi, E. *et al.* Design and Evaluation of Highly Selective Human Immunoproteasome Inhibitors Reveal a Compensatory Process That Preserves Immune Cell Viability. *J. Med. Chem.* **62**, 7032–7041 (2019).
32. Santos, R. de L. A. *et al.* Structure of human immunoproteasome with a reversible and noncompetitive inhibitor that selectively inhibits activated lymphocytes. *Nat. Commun.* **8**, 1–11 (2017).
33. Sharon, M., Witt, S., Glasmacher, E., Baumeister, W. & Robinson, C. V. Mass spectrometry reveals the missing links in the assembly pathway of the bacterial 20 S proteasome. *J. Biol. Chem.* **282**, 18448–18457 (2007).
34. Taverner, T. *et al.* Subunit Architecture of Intact Protein Complexes from Mass Spectrometry and Homology Modeling [†]. *Acc. Chem. Res.* **41**, 617–627 (2008).
35. Marcoux, J. & Cianférani, S. Towards integrative structural mass spectrometry: Benefits from hybrid approaches. *Methods* **89**, 4–12 (2015).
36. Smith, L. M., Kelleher, N. L. & Consortium for Top Down Proteomics. Proteoform: a single term describing protein complexity. *Nat. Methods* **10**, 186–187 (2013).
37. Gersch, M. *et al.* A Mass Spectrometry Platform for a Streamlined Investigation of Proteasome Integrity, Posttranslational Modifications, and Inhibitor Binding. *Chem. Biol.* **22**, 404–411 (2015).
38. Lesne, J., Bousquet, M.-P., Marcoux, J. & Locard-Paulet, M. Top-Down and Intact Protein Mass Spectrometry Data Visualization for Proteoform Analysis Using VisioProt-MS. *Bioinforma. Biol. Insights* **13**, 1177932219868223 (2019).
39. Bouyssié, D. *et al.* HDX-Viewer: interactive 3D visualization of hydrogen-deuterium exchange data. *Bioinforma. Oxf. Engl.* (2019) doi:10.1093/bioinformatics/btz550.
40. Osmulski, P. A. & Gaczynska, M. Nanoenzymology of the 20S proteasome: Proteasomal actions are controlled by the allosteric transition. *Biochemistry* **41**, 7047–7053 (2002).
41. Osmulski, P. A., Hochstrasser, M. & Gaczynska, M. A Tetrahedral Transition State at the Active Sites of the 20S Proteasome is Coupled to Opening of the α-Ring Channel. *Struct. Lond. Engl. 1993* **17**, 1137–1147 (2009).
42. Huang, R., Pérez, F. & Kay, L. E. Probing the cooperativity of Thermoplasma acidophilum proteasome core particle gating by NMR spectroscopy. *Proc. Natl. Acad. Sci. U. S. A.* **114**, E9846–E9854 (2017).
43. Park, S. *et al.* Reconfiguration of the proteasome during chaperone-mediated assembly. *Nature* **497**, 512–516 (2013).
44. Arciniega, M., Beck, P., Lange, O. F., Groll, M. & Huber, R. Differential global structural changes in the core particle of yeast and mouse proteasome induced by ligand binding. *Proc. Natl. Acad. Sci. U. S. A.* **111**, 9479–9484 (2014).
45. Whitby, F. G. *et al.* Structural basis for the activation of 20S proteasomes by 11S regulators. *Nature* **408**, 115–120 (2000).
46. Förster, A., Masters, E. I., Whitby, F. G., Robinson, H. & Hill, C. P. The 1.9 \AA Structure of a Proteasome-11S Activator Complex and Implications for Proteasome-PAN/PA700 Interactions. *Mol. Cell* **18**, 589–599 (2005).
47. Peitsch, M. C. ProMod and Swiss-Model: Internet-based Tools for Automated Comparative Protein Modelling. *Man. C Peitsch 1996 ProMod Swiss-Model Internet-Based Tools Autom. Comp. Protein Model. Chem. Des. Autom. News 11 1 13-14* **1**, 13–14 (1996).
48. Raule, M., Cerruti, F. & Cascio, P. Enhanced rate of degradation of basic proteins by 26S immunoproteasomes. *Biochim. Biophys. Acta BBA - Mol. Cell Res.* **1843**, 1942–1947 (2014).
49. Pickering, A. M. & Davies, K. J. A. Differential roles of proteasome and immunoproteasome regulators Pa28αβ, Pa28γ and Pa200 in the degradation of oxidized proteins. *Arch. Biochem. Biophys.* **523**, 181–190 (2012).

50. Jonik-Nowak, B. *et al.* PIP30/FAM192A is a novel regulator of the nuclear proteasome activator PA28γ. *Proc. Natl. Acad. Sci. U. S. A.* **115**, E6477–E6486 (2018).
51. Welk, V. *et al.* Inhibition of proteasome activity induces formation of alternative proteasome complexes. *J. Biol. Chem.* **291**, 13147–13159 (2016).
52. Sheff, J. G., Hepburn, M., Yu, Y., Lees-Miller, S. P. & Schriemer, D. C. Nanospray HX-MS configuration for structural interrogation of large protein systems. *The Analyst* **142**, 904–910 (2017).
53. Marcoux, J. *et al.* p47phox molecular activation for assembly of the neutrophil NADPH oxidase complex. *J. Biol. Chem.* **285**, 28980–28990 (2010).
54. Sowole, M. A., Alexopoulos, J. A., Cheng, Y.-Q., Ortega, J. & Konermann, L. Activation of ClpP Protease by ADEP Antibiotics: Insights from Hydrogen Exchange Mass Spectrometry. *J. Mol. Biol.* **425**, 4508–4519 (2013).
55. van de Waterbeemd, M. *et al.* Structural Analysis of a Temperature-Induced Transition in a Viral Capsid Probed by HDX-MS. *Biophys. J.* **112**, 1157–1165 (2017).
56. Sbardella, D. *et al.* The insulin-degrading enzyme is an allosteric modulator of the 20S proteasome and a potential competitor of the 19S. *Cell. Mol. Life Sci.* 1–16 (2018) doi:10.1007/s00018-018-2807-y.
57. Akiyama, K. *et al.* Replacement of proteasome subunits X and Y by LMP7 and LMP2 induced by interferon-gamma for acquirement of the functional diversity responsible for antigen processing. *FEBS Lett.* **343**, 85–8 (1994).
58. Stohwasser, R., Salzmann, U., Giesebrecht, J., Kloetzel, P.-M. & Holzhütter, H.-G. Kinetic evidences for facilitation of peptide channelling by the proteasome activator PA28. *Eur. J. Biochem.* **267**, 6221–6230 (2000).
59. Sugiyama, M. *et al.* Spatial arrangement and functional role of α subunits of proteasome activator PA28 in hetero-oligomeric form. *Biochem. Biophys. Res. Commun.* **432**, 141–145 (2013).
60. Fabre, B. *et al.* Deciphering preferential interactions within supramolecular protein complexes: the proteasome case. *Mol. Syst. Biol.* **11**, 771 (2015).
61. Olshina, M. A. *et al.* Regulation of the 20S Proteasome by a Novel Family of Inhibitory Proteins. *Antioxid. Redox Signal.* **32**, 636–655 (2020).
62. Goddard, T. D. *et al.* UCSF ChimeraX: Meeting modern challenges in visualization and analysis. *Protein Sci. Publ. Protein Soc.* **27**, 14–25 (2018).
63. Perez-Riverol, Y. *et al.* The PRIDE database and related tools and resources in 2019: improving support for quantification data. *Nucleic Acids Res.* **47**, D442–D450 (2019).

Acknowledgments

This work was supported by the French Ministry of Research (ANR-ProteasoRegMS to J.M and Investissements d'Avenir Program, Proteomics French Infrastructure, ANR-10-INBS-08 to O.B.-S.), the Fonds Européens de Développement Régional Toulouse Métropole and the Région Midi-Pyrénées (O.B.-S.) and the Novo Nordisk Foundation (NNF14CC0001).

Author contributions

All authors contributed to editing the manuscript and figures. J.L. performed the HDX-MS optimization and data acquisition, model building and data analysis. J.P. performed the HDX-MS optimization, data acquisition and data analysis. D.Z. performed experiments. M.L.P. analysed the data and wrote the paper. Odile Schiltz provided critical input. M.P.B. provided critical expertise on the proteasome. J.M. designed, performed and supervised the experiments, data and structural analysis, and wrote the paper.

Competing interests

The authors declare no competing interests.